On the influence of pressure, phase transitions, and water on large-scale seismic anisotropy underneath a subduction zone

J. K. Magali[1,2], C. Thomas[1], E. E. Ledoux[3], Y. Capdeville[4], S. Merkel[2]

[1]Institute of Geophysics, University of M¨unster, Corrensstr. 24, 48149 M¨unster, Germany'
[2]Univ. Lille, CNRS, INRAE, Centrale Lille, UMR 8207 - UMET - Unit´e Mat´eriaux et Transformations,
F-59000 Lille, France
[3]Department of Geology and Geophysics, University of Utah, Salt Lake City, UT, USA
[4]Laboratoire de Plan´etologie et G´eodynamique, CNRS, UMR 6112, Universit´e de Nantes, Nantes, France

email: jkvmagali@gmail.com
email #2: jmagali@uni-muenster.de

This manuscript is submitted for publication to *Geophysical Research Letters*

On the influence of pressure, phase transitions, and water on large-scale seismic anisotropy underneath a subduction zone

John Keith Magali[1,2], Christine Thomas[1], Estelle Elisa Ledoux[3], Yann Capdeville[4], Sébastien Merkel[2]

[1]Institute of Geophysics, University of Münster, Corrensstr. 24, 48149 Münster, Germany
[2]Univ. Lille, CNRS, INRAE, Centrale Lille, UMR 8207 - UMET - Unité Matériaux et Transformations, F-59000 Lille, France
[3]Department of Geology and Geophysics, University of Utah, Salt Lake City, UT, USA
[4]Laboratoire de Planétologie et Géodynamique, CNRS, UMR 6112, Université de Nantes, Nantes, France

Key Points:

- Geodynamic subduction model with experiment-informed mantle fabric transitions.
- $P-$dependent olivine textures can explain the evolution of upper mantle anisotropy.
- A relatively wet upper transition zone could likely explain faster V_{SV} than V_{SH} speeds.

Corresponding author: John Keith Magali, jkvmagali@gmail.com

Corresponding author: Sébastien Merkel, sebastien.merkel@univ-lille.fr

Abstract

Seismic anisotropy mainly originates from the crystallographic preferred orientation (CPO) of minerals deformed in the convective mantle flow. While fabric transitions have been previously observed in experiments, their influence on large-scale anisotropy is not well-documented. Here, we implement 2D geodynamic models of intra-oceanic subduction coupled with mantle fabric modelling to investigate the combined effect of pressure (P)- and water-dependent microscopic flow properties of upper mantle and upper transition zone (UTZ) minerals, respectively, on large-scale anisotropy. Our results for the upper mantle correlate well with observations, implying that the P-dependence of olivine fabrics is sufficient to explain the variability of anisotropy. Meanwhile, a dry UTZ tends to be near-isotropic whereas a relatively wet UTZ could produce up to 1% azimuthal and $\sim 2\%$ radial anisotropy. Because water facilitates CPO development, it is therefore likely a requirement to explain the presence of anisotropy in the transition zone close to subducting slabs.

Plain Language Summary

Subduction causes the surrounding mantle to deform according to the movement and pressure exerted by the plates. This influences the alignment of minerals making up the mantle, which in turn, affects the speed and direction of seismic waves known as seismic anisotropy. In this study, we investigate the role of pressure in the upper mantle and water in the transition zone on large-scale seismic anisotropy across a subduction zone. In the upper mantle, we show that the patterns of anisotropy at places where deformation is presumed to be large are affected by changes in pressure. In the transition zone, anisotropy tends to favour a wetter environment.

1 Introduction

Understanding subduction dynamics is crucial as it regulates, to first order, the coupling between deep mantle convection and surface deformation. Changes in mineralogy and viscosity structure at designated mantle transition zone boundaries control the style of subduction, and to some extent, the overall dynamics of plate tectonics (Agrusta et al., 2017; Goes et al., 2017). A plethora of geophysical observables can be used to constrain mantle flow; one of them is seismic anisotropy.

Seismic anisotropy mainly results from the crystallographic preferred orientation (CPO) in intrinsically anisotropic minerals upon progressive deformation along convective flows (Long & Becker, 2010). The parameters ξ for $S-$wave radial anisotropy (i.e., the ratio of the squares of V_{SH} and V_{SV} for horizontally-propagating $S-$waves) and a_z for azimuthal anisotropy (i.e., directional-dependence of V_{SV}) are simple yet intuitive ways of quantifying seismic anisotropy, and hence, are often constrained in tomographic imaging (e.g. Smith & Dahlen, 1973; Montagner, 1998; Panning & Romanowicz, 2006). In a subduction zone, the mantle wedge is characterized by a layer of positive radial anisotropy $\xi > 1$ (e.g. French & Romanowicz, 2014; Chang et al., 2015; Simmons et al., 2021) and $2-3\%$ peak-to-peak azimuthal anisotropy (e.g. Yuan & Beghein, 2013; Debayle et al., 2016). Underneath the oceanic lithosphere away from the slab, the patterns of anisotropy appear less complex exhibiting an age-independent distribution of $\xi > 1$ and $a_{V_{SV}}$ 2% with maximum amplitudes appearing at ~ 150 km (e.g. Yuan & Beghein, 2013; Debayle et al., 2016; Chang et al., 2015). Reduction of seismic anisotropy is observed past ~ 250 km depth (e.g. Nettles & Dziewoński, 2008; Burgos et al., 2014). Across the upper transition zone (UTZ, $410-520$ km) around slabs, $\xi < 1$ and $a_{V_{SV}} \sim 1-2\%$ is generally observed (e.g. Montagner et al., 2021).

The prevalent seismic anisotropy observed around subduction zones may be attributed either in terms of large strains that the entrained mantle adjacent to the slab experiences (Mainprice, 2010), structural layering of plate remnants (Karato, 1998), or possibly an interplay of both. Understanding the origin of anisotropy requires a multidisciplinary approach involving geodynamic modelling with mineral physics constraints. Such methods have already been carried out in the previous decade (e.g. Faccenda, 2014; Sturgeon et al., 2019) with some even accounting for the effect of small-scale isotropic heterogeneities (Faccenda et al., 2019; Ferreira et al., 2019; Magali et al., 2021). Yet, the impact of fabric transitions onto large-scale seismic anisotropy which has been observed experimentally in mineral microstructures (e.g. Mainprice et al., 2005; Raterron et al., 2007), is not fully investigated for realistic flows, especially in a subduction setting where strains are large. While certain mantle conditions must be met to induce fabric transitions, we focus on the effect of pressure in the upper mantle and water in the UTZ based on previous findings that $P-$induced olivine slip transitions and water in the UTZ strongly influence the depth distribution of the observed radial anisotropy (Magali et al., 2024). For simplicity, we will not consider the effect of water on upper mantle anisotropy.

Here, we build upon previous CPO modelling studies (e.g. Faccenda, 2014; Li et al., 2014; Sturgeon et al., 2019; Fraters & Billen, 2021) by integrating mantle fabric transitions to predict radial and azimuthal anisotropy underneath a subduction zone. We then apply elastic homogenization (Capdeville et al., 2015; Capdeville & Métivier, 2018) as a post-processing step, and compare the effective anisotropy with anisotropic tomography models across the Honshu arc. Two main problems will be addressed using our modelling strategy: (i) Determine whether $P-$induced slip transitions in olivine could sufficiently explain the variability of anisotropy in the upper mantle, and (ii) investigate the role of water in the development of anisotropy in the UTZ using the recently published texture data of wadsleyite (Ohuchi et al., 2014; Ledoux et al., 2023a).

2 Methods

We carry out 2D 6000 km$\times$1000 km thermo-chemical modelling of intra-oceanic subduction with phase transformations using the open software ASPECT (Kronbichler et al., 2012) (Figure S1a of Supplementary Text S1). The transition zone is characterized by phase transformations of olivine polymorphs that may either inhibit or assist subduction: olivine to wadsleyite at $\sim$410 km, wadsleyite to ringwoodite at $\sim$520 km and finally ringwoodite to bridgmanite at $\sim$660 km (Figure 1). As we are only interested in upper mantle and UTZ anisotropy, we limit our modelling to a slab stagnating at 660 km. We employ `Perple_X` (Connolly, 2005, 2009) coupled with the recently published thermodynamic database of Stixrude and Lithgow-Bertelloni (2022) to estimate the density ρ as a function of P and T assuming a pyrolitic mantle. Phase transition boundary topography in the subduction model is inferred from the density map (Figure S2).

2.1 Mantle fabric modelling

Starting at the initial step along a pathline followed by a tracer, we estimate the local velocity gradient $\mathbf{L}'$, local total pressure (hydrostatic + dynamic) P', and local temperature T' by introducing a new velocity, total pressure, and temperature fields at the current time step t from ASPECT. Local density ρ' along the pathline is estimated with the help of the density map (Figure S2a). At the final time step t_{final}, tracers are regularly distributed inside the white dashed rectangle of Figure S2c where anisotropy has been calculated. We use the full $\mathbf{L}'$ for strain accumulation.

To model mantle fabrics, we implement the modified viscoplastic self-consistent (VPSC) method of Lebensohn and Tomé (1993) that incorporates $P-$induced slip transitions and $P-$induced phase transformations (Magali et al., 2024). While kinematic models are less computationally demanding and can replicate large-scale anisotropy features (e.g. Kaminski et al., 2004), VPSC offers the capability to work with an arbitrary number of independent slip systems. Furthermore, it explicitly accounts for variations in intragranular stress and strain, resulting in more precise predictions of the mechanical behavior of deforming polycrystals (Castelnau et al., 2008). Each tracer with density ρ' is composed of 3000 initial randomly oriented grains with the following modal abundancies: Upper mantle ($\rho' < 3720\ \text{kg} \cdot \text{m}^{-3}$): 60% $P-$dependent olivine (Magali et al., 2024) and 40%

other phases (assumed isotropic), UTZ ($3720 \leq \rho' < 3850$ kg $\cdot$ m^{-3}): 60% wadsleyite (Ledoux et al., 2023a) and 40% garnet, and lower transition zone (LTZ, $3850 \leq \rho' < 4170$ kg $\cdot$ m^{-3}): 60% ringwoodite and 40% garnet. Both garnet and ringwoodite are deemed isotropic (e.g. Mainprice, 2007). The single crystal elastic constants of the phases at ambient conditions, including their PT derivatives are listed in Magali et al. (2024). Wadsleyite properties are more complex to incorporate and will henceforth be discussed below.

2.2 An ersatz to compute water-dependent anisotropy in the transition zone

In this study, we assume that the ambient UTZ is dry and the slab, together with the entrained mantle, is relatively wet. To do this, tracers are specified with either hydrous (i.e., C_{wd}-type) or dry wadsleyite (i.e., B_{wd}-type) depending on their positioning relative to the slab (Ledoux et al., 2023a). Tracers with $T' < 1750$ K envelope the cold and slightly hydrated slab, and hence C_{wd}-type CPO is calculated. Consequently, those with $T' \geq 1750$ K are prescribed with a B_{wd}-type fabric. The latter corresponds to tracers scattered around the dry and ambient UTZ. We also test the effect of a fully dry UTZ by computing the CPO of B_{wd}-type wadsleyite aggregates across the entire UTZ.

P and $T-$dependent wadsleyite polycrystal elastic tensors are also computed using Voigt-Reuss-Hill averaging around their single crystal counterparts. Hydrous and dry elastic constants are inferred from Zhou et al. (2022) and Núñez-Valdez et al. (2013), respectively. Their PT derivatives are also listed in Magali et al. (2024). CPO of a tracer crossing a phase transition boundary determined by the density crossovers is erased and instead replaced with random textures according to experimental results of microstructures induced by the olivine → wadsleyite transition (Smyth et al., 2012; Ledoux et al., 2023b). Anisotropy calculations are ceased past $\rho' = 4150$ kg $\cdot$ m^{-3} (i.e., 660 km). Mineral assignments are summarized in Figure 1.

2.3 Elastic homogenization

For a realistic comparison with anisotropic tomography models, we first apply the fast-Fourier homogenization (FFH) algorithm (Capdeville et al., 2010, 2015) to obtain an effective medium void of spatial heterogeneities whose scales are much smaller than the minimum wavelength λ_0 of the observed wavefield. The result is a smooth tomographic version of the elastic medium, similar to an image recovered by full waveform inversion assuming perfect data coverage (Capdeville & Métivier, 2018). Finally, we apply the elastic decomposition method of Montagner and Nataf (1986) to compute radial anisotropy and azimuthal anisotropy (Supplementary Texts S3 and S4).

3 Results

3.1 Predictions of large-scale upper mantle anisotropy induced by subduction

The influence of $P-$induced slip transitions on anisotropy can be observed in the subslab mantle (Figures 2a and 3a). Here, anisotropy strength decreases with depth; dropping to $\xi \sim 1.01$ and $a_z \sim 1\%$ at $z = 400$ km. The presumed switch in primary activities from the [100](010) to the [001](010) slip systems may have caused this (Raterron et al., 2014; Magali et al., 2024), as also evidenced by the slight re-alignment of the [100] axes towards the (010) direction (Figure S3e-g). The mantle wedge mainly exhibits positive radial anisotropy $\xi > 1$ and nonzero azimuthal anisotropy $a_z \sim 5\%$. However, the entrained mantle immediately beneath the back-arc basin ($z \sim 90 - 150$ km) experiences rapid trench retreat motion due to a decreased upper plate forcing of a thin overriding lithosphere (Agrusta et al., 2017). This creates a localized region of complex anisotropy patterns with $\xi < 1$ and $a_z < 5\%$. Negative radial anisotropy ($\xi \sim 0.97$) and near-zero azimuthal anisotropy are generated just above the upper transition zone (UTZ) close to the slab ($\sim 290-400$ km). At these depths, the lateral extent x of subhorizontal FSE orientations cover $\sim$ 2000 km $\leq x \leq$ 3200 km (Figure 1b). Li et al.

(2014) revealed aggregates submitted to subduction zone stresses exhibit olivine [100] axes that are approximately aligned with the FSE long axis. The existence of a negative radial anisotropy $\xi < 1$ at these depths, where the fast directions are now sub-normal to the FSE, is also indicative of $P-$induced slip transitions in olivine.

3.2 Effect of water around the slab on mantle transition zone anisotropy

A wet UTZ near the slab is generally characterized by an accumulation of negative radial anisotropy with $\xi \sim 0.97$ above the slab and $\xi \sim 0.98$ in the subslab area (Figure 2a). A localized area of weak positive radial anisotropy ($\xi \sim 1.01$) forms close to the slab tip which can be attributed to the preferential alignment of the [100] axes of the $\mathrm{C_{wd}}-$type phase with the horizontal (Figure S3h) in response to rapid changes in the deformation patterns of the entrained mantle close to the slab tip. Small amounts of azimuthal anisotropy $a_Z \sim 1.1\%$ far from the slab tip and up to $a_Z \sim 1\%$ in the remaining regions close to the slab can be found (Figure 3a).

Figures 2b and 3b show the results of the same calculations assuming a fully dry transition zone (i.e., $\mathrm{B_{wd}}$-type texture and elastic constants retrieved from Núñez-Valdez et al. (2013)). Such an assumption leads to an almost isotropic UTZ around the slab. $a_Z \sim 1.1\%$ away from the slab tip can also be detected which means that dry fabrics can produce enough azimuthal anisotropy but may fail to generate observable radial anisotropy.

3.3 Comparison with tomographic observations: a case for the Honshu arc

We select cross-sections of radial anisotropy and azimuthal anisotropy from SGLOBE-Rani (Chang et al., 2015) and 3DLGL-TPESv.v2022-11 (Debayle et al., 2016), respectively, for the Honshu subduction zone which, to some extent, displays a similar geometry and subduction style to our model. For comparison, we solely homogenize the CPO model with a wet UTZ since we find that no substantial anisotropy is developed assuming a fully dry UTZ, contrary to tomographic observations where anisotropy is present around slabs (e.g. Chang et al., 2015; Debayle et al., 2016; Montagner et al., 2021). Supplementary Figures S4 and S5 show the effective anisotropy models at different homogenization wavelengths λ_0.

3.3.1 Effective radial anisotropy ($\lambda_0 = 65$ km) comparison with SGLOBE-Rani

To get the effective radial anisotropy ξ^* comparable to SGLOBE-Rani, we choose a homogenization wavelength of $\lambda_0 = 65$ km (Figure 2c). Localized areas of the observed negative radial anisotropy $\xi_{\text{obs}} < 1$ underneath the back-arc basin and just above the stagnant slab is evident (Figure 2d). Whether these peculiar features are robust or not, however, warrants regional tomography for better resolution. Nonetheless, their presence can be reproduced with a geodynamic model that accounts for transient flows and P-dependent fabrics in olivine (Figures 2c; 2e red and green dashed lines). Across the subslab mantle, the decrease in ξ^* with depth correlates well with observations. In the UTZ, modelling with wet wadsleyite fabrics captures the persistence of $\xi_{\text{obs}} < 1$ near the slab. $P-$induced phase transformations from olivine to wadsleyite at $\sim$410 km, and to ringwoodite at $\sim$520 km introduce sharp velocity contrasts that when homogenized, produce a thin layer of weak $\xi^* > 1$ which is not observed in SGlobe-Rani. Finally, ξ^* cannot explain the prevalence of ξ_{obs} in the LTZ. Small-scale heterogeneities unaccounted for in our model such as petrological layering of transformed subducted material could explain such observations (Karato, 1998). Smearing effects from the tomographic inversion could also lead to the presence of radial anisotropy in the LTZ.

3.3.2 Effective azimuthal anisotropy ($\lambda_0 = 164$ km) comparison with 3DLGL-TPESv.v2022-11

Choosing a longer homogenization wavelength ($\lambda_0 \sim 165$ km) intensifies the spatial averaging of small-scale heterogeneities in azimuthal anisotropy (Figure 3c). This leads to a decrease in azimuthal anisotropy of about 1%. Comparison with the 3DLGL-

TPESv.v2022-11 tomographic model (Figure 3d) is not as robust as with our result from ξ^* with SGlobe-Rani. For instance, the consistent azimuthal anisotropy at depths above ~ 250 km predicted from our model only appears in patches in 3DLGL-TPESv.v2022-11. Furthermore, the predicted anisotropy in the UTZ is significantly underestimated (Figure 3e). Several factors may be involved in the difference between a_z^* and a_z^{obs}. The first may be related to ad-hoc constraints on regularization where the spatial distribution of a_z^{obs} is bounded to this uncertainty. Another factor relates to the dimensionality of our model. Here, although the elastic tensors computed from VPSC are in 3D, the latter relies on a 2D representation of thermo-chemical subduction. Thus, toroidal flow was not taken into account which was shown to participate in the production of trench-parallel anisotropy (Faccenda & Capitanio, 2012, 2013; Li et al., 2014), and hence a rather complex distribution of azimuthal anisotropy (e.g. Rychert et al., 2012).

4 Discussion

4.1 Pressure-dependence of single-phase fabrics and its implications for the upper mantle

Laboratory studies have already reported the existence of pressure-dependence of olivine microstructures (Mainprice et al., 2005; Raterron et al., 2007; Jung et al., 2009; Ohuchi et al., 2011), and most recently of bridgmanite (Gay et al., 2024). To this day, however, it is still not clear how textures evolve with hydrostatic pressure (Karato et al., 2008) since high-P experiments are also characterized by high differential stresses $\sigma \sim 100-500$ MPa which could contribute to fabric transitions (e.g. Katayama et al., 2004). Deformed peridotites extracted from xenoliths gathered mostly from the Western US, however, recorded lower differential stresses of about ~ 30 MPa (Bernard et al., 2019). Under low σ, Raterron et al. (2012) numerically demonstrated using the first-principles approach of Durinck et al. (2007) the slip transition from [100](010) to [001](010) olivine slip system in the deep upper mantle; consistent with Raterron et al. (2007); Jung et al. (2009); Ohuchi et al. (2011).

4.1.1 Can $P-$induced slip transitions be used as a proxy to describe the alphabet fabrics (i.e, A-, B-, C-, and E-type olivine)?

The response of strain-induced anisotropy on pressure becomes more evident in regions associated with large deformation (Magali et al., 2024); in our model, across the mantle wedge and the subslab mantle where the entrained mantle experiences first-hand the influence of slab pull. At low pressures, our implementation of $P-$induced olivine fabric transitions emulates an A-type fabric because of increased activities at the [100](010) slip system. At high pressures, it somehow follows a B-type fabric due to the switch in primary activities to the [001](010) slip system (Raterron et al., 2012, 2014). While $P-$induced apparent B-type fabrics could explain the distribution of anisotropy around the slab at high pressures, we could also not dismiss the effect of water on the generation of such fabric at low confining pressures (Ohuchi et al., 2012). Proxies of a water-rich environment in the convective flow are required to differentiate the possible origin (i.e. $P-$induced or water-induced) of B-type fabrics; although there is still no apparent relationship between olivine fabric types and water fugacity (Bernard et al., 2019).

Different conditions must be met to derive a suite of fabrics other than A- and B-type. Under low stresses and at increasing temperatures and a relatively dry mantle, an A-type transitions to an E-type[1] fabric, and increasing water content, to a C-type[2] fabric (Karato et al., 2008). Results from geodynamic simulations of upper mantle flow suggest $\xi > 1$ for A, B, and E-type fabrics, with E-type exhibiting minimal strength, whereas $\xi < 1$ for C-type, in the case of horizontal simple shear. As for a_z, all except B-type exhibit fast propagation directions parallel to the direction of shear (Long & Becker, 2010).

[1] easiest slip system at [100](001)
[2] easiest slip system at [001](100)

While it is tempting to infer the potential distribution of such fabrics across a subduction zone based on the distribution of ξ and a_z, doing so requires an extension of a depth-dependent model for anisotropy. Therefore, $P-$dependent olivine cannot be used as a proxy to describe fabric types. Lateral dependence can be accomplished by tracking the effect of temperature and differential stresses on olivine slip systems CRSS, for example, using first-principle calculations coupled with the Peierls–Nabarro formalism for olivine plasticity (e.g. Durinck et al., 2007). Nevertheless, we anticipate that classifying fabrics using large-scale anisotropy models alone would be difficult to execute. For better classification, textures derived from old fabrics must be completely overwritten by newer textures developed from a set of CRSS that reflect the current fabric.

4.1.2 On the reduction of free-parameters to constrain patterns of large-scale anisotropy

In recent years, models of upper mantle anisotropy are derived from carefully chosen methodologies such as: (a) implementation of a two-phase aggregate composed of 60% olivine and 40 % enstatite reminiscent of a pyrolitic mantle (Ringwood, 1991), (b) strain partitioning where a fraction accommodated by dislocation creep is used for CPO development consistent with Karato and Wu (1993), and (c) the extension of homogenization methods for CPO modelling by incorporating dynamic recrystallization. Several studies have applied such methodologies in a subduction setting where the variability of radial anisotropy has been correctly predicted in certain places (Faccenda & Capitanio, 2012; Faccenda, 2014; Sturgeon et al., 2019; Ferreira et al., 2019). Implementation of such methodologies, however, becomes increasingly difficult due to the sheer amount of free parameters that control the variability of anisotropy. This is not to say that these methods should not be implemented given that such values can be obtained from literature. However, a more grounded approach should not be ruled out either. We argue that a simple depth-dependent anisotropy of single-phase aggregates, without the need for strain partitioning and additional mechanisms for CPO development, is enough to explain the variability of large-scale anisotropy in the upper mantle. This is especially true given the uncertainty surrounding where dislocation creep should subjugate (Hirth & Kohlstedf, 2003; Becker & Lebedev, 2021) and the inability of seismic waves to distinguish deformation from recrystallization textures (Wenk & Tomé, 1999).

4.2 Importance of water on the variability of transition zone anisotropy

In light of our conducted numerical experiments, a relatively wet UTZ subjected to subduction stresses produces substantial radial anisotropy and about 1% azimuthal anisotropy. Contrastingly, a fully dry UTZ appears mostly isotropic. The anisotropy distribution in the hydrous model is thus consistent with source-side splitting observations surrounding deep earthquakes, particularly in the western Pacific (Nowacki et al., 2015; Mohiuddin et al., 2015). Our predictions, however, are not perfect, particularly a_z where its amplitude appears underestimated. Around slabs, Moulik and Ekström (2014) measured radial anisotropy of about $\xi \sim 1.04$ underneath the circum-Pacific region; whereas azimuthal anisotropy could reach up to $a_z \sim 3\%$ according to Huang et al. (2019). There are several propositions for the increased anisotropy around subduction zones aside from wadsleyite CPO. Local enrichment of akimotoite may be the leading cause for source-side shear wave splitting observations underneath stagnant slabs (Foley & Long, 2011). Dense hydrous magnesium silicates (DHMS) have also been shown to be very anisotropic at UTZ conditions (Nowacki et al., 2015) but their abundance and stability remain inconclusive (Hao et al., 2020). Although Nowacki et al. (2015) suggested shape preferred orientation may contribute to the development of anisotropy, this may be unlikely since elliptical inclusions must be periodically aligned vertically to match $\xi < 1$ around subduction zones where horizontal laminations are more rampant instead (Faccenda et al., 2019; Magali et al., 2021). Furthermore, neither metastable olivine nor topotactical relationships between olivine and wadsleyite could be possible candidates due to their unlikely existence in hydrous environments (Smyth et al., 2012). It is thus plausible that the amount of effective strains in our models did not achieve that of actual subduction systems, and that our 2D setting relegates the complexity of deformation patterns which would explain the discrepancy in anisotropy strength (McKenzie, 1979). Even so, we assert that the patterns of UTZ anisotropy we predict remain robust.

The incorporation of water in wadsleyite promotes CPO development and therefore captures the variability of anisotropy. This challenges the study of Chang and Ferreira (2019) where it is inferred that a dry UTZ is likely the cause of substantial radial anisotropy ($\xi \sim 1.02 - 1.03$) across slabs underneath the western Pacific. While a dry single crystal wadsleyite indeed contains larger intrinsic anisotropy, Zhou et al. (2022) reported anisotropy increases with water content in the case of deformed wadsleyite aggregates, primarily due to increased crystallographic defects that weaken its rheology. With enough deformation accumulated in the UTZ, we model, for the first time, the dependence of the distribution of large-scale anisotropy on water. The relatively misunderstood effect of strong accumulation, however, precludes the prediction of anisotropy strength with the degree of hydration in the UTZ. Further analyses are imperative to reconcile seismic observations (e.g. Chang & Ferreira, 2019) and mineralogical experiments (e.g. Ohuchi et al., 2014; Zhou et al., 2022) with the help of additional constraints such as electrical conductivity measurements (Kelbert et al., 2009; Karato, 2011).

5 Conclusion

We have integrated pressure(P)-induced olivine fabric transitions and $P-$induced phase transformations in CPO calculations to predict the distribution of large-scale anisotropy around a subduction zone. Coupled with an elastic homogenization algorithm that acts as a tomographic filter, depth-dependent anisotropy of a single-phase fabric is enough to capture the variability of the observed anisotropy in the upper mantle. Strain partitioning, modelling of multi-phase aggregates, and implementations of other potential mechanisms for CPO development may not be warranted; reducing the number of free parameters that need to be constrained. In the upper transition zone (UTZ), the CPO of deformed hydrous wadsleyite is likely the leading cause for the observed anisotropy near the subducting slab. This opens a fresh perspective on how water is integral to its deformation history. Discrepancies in the strength of anisotropy, however, remain an open question. Further challenges therefore await such as identifying an empirical relationship between the amount of water and the strength of anisotropy in deformed aggregates.

Open Research Section

Subduction flow modelling was done using the open software ASPECT (`https://aspect.geodynamics.org/`), and fabric calculations were performed using VPSC (`https://github.com/lanl/VPSC_code`) The Fast Fourier Homogenization (FFH) code can be made available upon reasonable request to Y. Capdeville. Its foundation is based upon the following in-text citation references: (Capdeville et al., 2015) and (Capdeville & Métivier, 2018). This study is entirely numerical. The input files for Aspect and VPSC, useful routines for calculating single crystal elastic constants and CRSS as a function of P and T, and output elastic tensor files can be found in `https://doi.org/10.5281/zenodo.12774418`.

Acknowledgments

The study was funded by the bilateral ANR-DFG TIMEleSS project (ANR-17-CE31-0025; TH 1530/18-1; SA 2585/3-1; SP1216/8-1), and by the DFG LASSIE project (TH1530/24-1). Computations were performed in the in-house PALMA cluster of the University of Münster.

References

Agrusta, R., Goes, S., & Van Hunen, J. (2017). Subducting-slab transition-zone interaction: Stagnation, penetration and mode switches. *Earth and Planetary Science Letters*, *464*, 10–23.

Becker, T. W., & Lebedev, S. (2021). Dynamics of the upper mantle in light of seismic anisotropy. *Mantle convection and surface expressions*, 257–282.

Bernard, R. E., Behr, W. M., Becker, T. W., & Young, D. J. (2019). Relationships between olivine cpo and deformation parameters in naturally deformed rocks and implications for mantle seismic anisotropy. *Geochemistry, Geophysics, Geosystems*, *20*(7), 3469–3494.

Burgos, G., Montagner, J.-P., Beucler, E., Capdeville, Y., Mocquet, A., & Drilleau, M. (2014). Oceanic lithosphere-asthenosphere boundary from surface wave dispersion data. *Journal of Geophysical Research: Solid Earth*, *119*(2), 1079–1093.

Capdeville, Y., Guillot, L., & Marigo, J.-J. (2010). 2-d non-periodic homogenization to upscale elastic media for p–sv waves. *Geophysical Journal International*, *182*(2), 903–922.

Capdeville, Y., & Métivier, L. (2018, 5). Elastic full waveform inversion based on the homogenization method: theoretical framework and 2-d numerical illustrations. *Geophysical Journal International*, *213*, 1093-1112. doi: 10.1093/gji/ggy039

Capdeville, Y., Zhao, M., & Cupillard, P. (2015, 4). Fast fourier homogenization for elastic wave propagation in complex media. *Wave Motion*, *54*, 170-186. doi: 10.1016/j.wavemoti.2014.12.006

Castelnau, O., Blackman, D., Lebensohn, R., & Ponte Castañeda, P. (2008). Micromechanical modeling of the viscoplastic behavior of olivine. *Journal of Geophysical Research: Solid Earth*, *113*(B9).

Chang, S.-J., & Ferreira, A. M. (2019). Inference on water content in the mantle transition zone near subducted slabs from anisotropy tomography. *Geochemistry, Geophysics, Geosystems*, *20*(2), 1189–1201.

Chang, S.-J., Ferreira, A. M., Ritsema, J., van Heijst, H. J., & Woodhouse, J. H. (2015). Joint inversion for global isotropic and radially anisotropic mantle structure including crustal thickness perturbations. *Journal of Geophysical Research: Solid Earth*, *120*(6), 4278–4300.

Connolly, J. A. (2005). Computation of phase equilibria by linear programming: a tool for geodynamic modeling and its application to subduction zone decarbonation. *Earth and Planetary Science Letters*, *236*(1-2), 524–541.

Connolly, J. A. (2009). The geodynamic equation of state: what and how. *Geochemistry, geophysics, geosystems*, *10*(10).

Debayle, E., Dubuffet, F., & Durand, S. (2016). An automatically updated s-wave model of the upper mantle and the depth extent of azimuthal anisotropy. *Geophysical Research Letters*, *43*(2), 674–682.

Durinck, J., Carrez, P., & Cordier, P. (2007). Application of the peierls-nabarro model to dislocations in forsterite. *European Journal of Mineralogy*, *19*(5), 631–639.

Faccenda, M. (2014). Mid mantle seismic anisotropy around subduction zones. *Physics of the Earth and Planetary Interiors*, *227*, 1–19.

Faccenda, M., & Capitanio, F. A. (2012). Development of mantle seismic anisotropy during subduction-induced 3-d flow. *Geophysical Research Letters*, *39*(11).

Faccenda, M., & Capitanio, F. A. (2013). Seismic anisotropy around subduction zones: Insights from three-dimensional modeling of upper mantle deformation and sks splitting calculations. *Geochemistry, Geophysics, Geosystems*, *14*(1), 243–262.

Faccenda, M., Ferreira, A. M., Tisato, N., Lithgow-Bertelloni, C., Stixrude, L., & Pennacchioni, G. (2019). Extrinsic elastic anisotropy in a compositionally heterogeneous earth's mantle. *Journal of Geophysical Research: Solid Earth*, *124*(2), 1671–1687.

Ferreira, A. M., Faccenda, M., Sturgeon, W., Chang, S.-J., & Schardong, L. (2019). Ubiquitous lower-mantle anisotropy beneath subduction zones. *Nature Geoscience*, *12*(4), 301–306.

Foley, B. J., & Long, M. D. (2011). Upper and mid-mantle anisotropy beneath the tonga slab. *Geophysical Research Letters*, *38*(2).

Fraters, M. R. T., & Billen, M. I. (2021). On the implementation and usability of cpo evolution in geodynamic modelling. *Earth and Space Science Open Archive ESSOAr*.

French, S., & Romanowicz, B. A. (2014). Whole-mantle radially anisotropic shear velocity structure from spectral-element waveform tomography. *Geophysical Journal International*, *199*(3), 1303–1327.

Goes, S., Agrusta, R., van Hunen, J., & Garel, F. (2017). Subduction-transition zone interaction: A review. *Geosphere*, *13*(3), 644–664.

Hao, M., Zhang, J. S., Pierotti, C. E., Zhou, W.-Y., Zhang, D., & Dera, P. (2020). The seismically fastest chemical heterogeneity in the earth's deep upper mantle—implications from the single-crystal thermoelastic properties of jadeite. *Earth and Planetary Science Letters*, *543*, 116345.

Hirth, G., & Kohlstedf, D. (2003). Rheology of the upper mantle and the mantle wedge: A view from the experimentalists. *Geophysical monograph-american geophysical union*, *138*, 83–106.

Huang, Q., Schmerr, N., Waszek, L., & Beghein, C. (2019). Constraints on seismic anisotropy in the mantle transition zone from long-period ss precursors. *Journal of Geophysical Research: Solid Earth*, *124*(7), 6779–6800.

Jung, H., Mo, W., & Green, H. W. (2009). Upper mantle seismic anisotropy resulting from pressure-induced slip transition in olivine. *Nature Geoscience*, *2*(1), 73–77.

Kaminski, E., Ribe, N. M., & Browaeys, J. T. (2004). D-rex, a program for calculation of seismic anisotropy due to crystal lattice preferred orientation in the convective upper mantle. *Geophysical Journal International*, *158*(2), 744–752.

Karato, S.-i. (1998). Seismic anisotropy in the deep mantle, boundary layers and the geometry of mantle convection. In *Geodynamics of lithosphere & earth's mantle* (pp. 565–587). Springer.

Karato, S.-i. (2011). Water distribution across the mantle transition zone and its implications for global material circulation. *Earth and Planetary Science Letters*, *301*(3-4), 413–423.

Karato, S.-i., Jung, H., Katayama, I., & Skemer, P. (2008). Geodynamic significance of seismic anisotropy of the upper mantle: New insights from laboratory studies. *Annu. Rev. Earth Planet. Sci.*, *36*, 59–95.

Karato, S.-i., & Wu, P. (1993). Rheology of the upper mantle: A synthesis. *Science*, *260*(5109), 771–778.

Katayama, I., Jung, H., & Karato, S.-i. (2004). New type of olivine fabric from deformation experiments at modest water content and low stress. *Geology*, *32*(12), 1045–1048.

Kelbert, A., Schultz, A., & Egbert, G. (2009). Global electromagnetic induction constraints on transition-zone water content variations. *Nature*, *460*(7258), 1003–1006.

Kronbichler, M., Heister, T., & Bangerth, W. (2012). High accuracy mantle convection simulation through modern numerical methods. *Geophysical Journal International*, *191*(1), 12–29.

Lebensohn, R. A., & Tomé, C. (1993). A self-consistent anisotropic approach for the simulation of plastic deformation and texture development of polycrystals: application to zirconium alloys. *Acta metallurgica et materialia*, *41*(9), 2611–2624.

Ledoux, E. E., Krug, M., Gay, J., Chantel, J., Hilairet, N., Bykov, M., … others (2023b). In-situ study of microstructures induced by the olivine to wadsleyite transformation at conditions of the 410 km depth discontinuity. *American Mineralogist*, *108*(12), 2283–2293.

Ledoux, E. E., Saki, M., Gay, J. P., Krug, M., Castelnau, O., Zhou, W.-Y., … others (2023a). Deformation mechanisms, microstructures, and seismic anisotropy of wadsleyite in the earth's transition zone. *Geochemistry, Geophysics, Geosystems*, *24*(11), e2023GC011026.

Li, Z. H., Di Leo, J. F., & Ribe, N. M. (2014). Subduction-induced mantle flow, finite strain, and seismic anisotropy: Numerical modeling. *Journal of Geophysical Research: Solid Earth*, *119*(6), 5052–5076.

Long, M. D., & Becker, T. W. (2010). Mantle dynamics and seismic anisotropy. *Earth and Planetary Science Letters*, *297*(3-4), 341–354.

Magali, J. K., Bodin, T., Hedjazian, N., Ricard, Y., Capdeville, Y., & Debayle, E. (2021). Quantifying intrinsic and extrinsic contributions to radial anisotropy in tomographic models. *Journal of Geophysical Research: Solid Earth*, *126*(10), e2021JB022322.

Magali, J. K., Ledoux, E. E., Thomas, C., Capdeville, Y., & Merkel, S. (2024, 05). Pressure-dependent large-scale seismic anisotropy induced by non-Newtonian mantle flow. *Geophysical Journal International*, ggae165. Retrieved from `https://doi.org/10.1093/gji/ggae165` doi: 10.1093/gji/ggae165

Mainprice, D. (2007). *Seismic anisotropy of the deep earth from a mineral and rock physics perspective, treatise geophys., 2, 437–491, doi: 10.1016* (Tech. Rep.). B978-044452748-6.00045-6.

Mainprice, D. (2010). 2.16 seismic anisotropy of the deep earth from a mineral and rock physics perspective. *Treatise on Geophysics, Volume 2: Mineral Physics*, 437.

Mainprice, D., Tommasi, A., Couvy, H., Cordier, P., & Frost, D. J. (2005). Pressure sensitivity of olivine slip systems and seismic anisotropy of earth's upper mantle. *Nature*, *433*(7027), 731–733.

McKenzie, D. (1979). Finite deformation during fluid flow. *Geophysical Journal International*, *58*(3), 689–715.

Mohiuddin, A., Long, M. D., & Lynner, C. (2015). Mid-mantle seismic anisotropy beneath southwestern pacific subduction systems and implications for mid-mantle deformation. *Physics of the Earth and Planetary Interiors*, *245*, 1–14.

Montagner, J.-P. (1998). Where can seismic anisotropy be detected in the earth's mantle? in boundary layers... *Pure and Applied Geophysics*, *151*(2), 223–256.

Montagner, J.-P., Burgos, G., Capdeville, Y., Beucler, E., & Mocquet, A. (2021). The mantle transition zone dynamics as revealed through seismic anisotropy. *Tectonophysics*, *821*, 229133.

Montagner, J.-P., & Nataf, H.-C. (1986). A simple method for inverting the azimuthal anisotropy of surface waves. *Journal of Geophysical Research: Solid Earth*, *91*(B1), 511–520.

Moulik, P., & Ekström, G. (2014). An anisotropic shear velocity model of the earth's mantle using normal modes, body waves, surface waves and long-period waveforms. *Geophysical Journal International*, *199*(3), 1713–1738.

Nettles, M., & Dziewoński, A. M. (2008). Radially anisotropic shear velocity structure of the upper mantle globally and beneath north america. *Journal of Geophysical Research: Solid Earth*, *113*(B2).

Nowacki, A., Kendall, J.-M., Wookey, J., & Pemberton, A. (2015). Mid-mantle anisotropy in subduction zones and deep water transport. *Geochemistry, Geophysics, Geosystems*, *16*(3), 764–784.

Núñez-Valdez, M., Wu, Z., Yu, Y., & Wentzcovitch, R. (2013). Thermal elasticity of (fex, mg1- x) 2sio4 olivine and wadsleyite. *Geophysical Research Letters*, *40*(2), 290–294.

Ohuchi, T., Fujino, K., Kawazoe, T., & Irifune, T. (2014). Crystallographic preferred orientation of wadsleyite and ringwoodite: Effects of phase transformation and water on seismic anisotropy in the mantle transition zone. *Earth and Planetary Science Letters*, *397*, 133–144.

Ohuchi, T., Kawazoe, T., Nishihara, Y., & Irifune, T. (2012). Change of olivine a-axis alignment induced by water: Origin of seismic anisotropy in subduction zones. *Earth and Planetary Science Letters*, *317*, 111–119.

Ohuchi, T., Kawazoe, T., Nishihara, Y., Nishiyama, N., & Irifune, T. (2011). High pressure and temperature fabric transitions in olivine and variations in upper mantle seismic anisotropy. *Earth and Planetary Science Letters*, *304*(1-2), 55–63.

Panning, M., & Romanowicz, B. (2006). A three-dimensional radially anisotropic model of shear velocity in the whole mantle. *Geophysical Journal International*, *167*(1), 361–379.

Raterron, P., Chen, J., Li, L., Weidner, D., & Cordier, P. (2007). Pressure-induced slip-system transition in forsterite: Single-crystal rheological properties at mantle pressure and temperature. *American Mineralogist*, *92*(8-9), 1436–1445.

Raterron, P., Detrez, F., Castelnau, O., Bollinger, C., Cordier, P., & Merkel, S. (2014). Multiscale modeling of upper mantle plasticity: From single-crystal rheology to multiphase aggregate deformation. *Physics of the Earth and Planetary Interiors*, *228*, 232–243.

Raterron, P., Girard, J., & Chen, J. (2012). Activities of olivine slip systems in the upper mantle. *Physics of the Earth and Planetary Interiors*, *200*, 105–112.

Ringwood, A. E. (1991). Phase transformations and their bearing on the constitution and dynamics of the mantle. *Geochimica et Cosmochimica Acta*, *55*(8), 2083–2110.

Rychert, C. A., Schmerr, N., & Harmon, N. (2012). The pacific lithosphere-asthenosphere boundary: Seismic imaging and anisotropic constraints from ss waveforms. *Geochemistry, Geophysics, Geosystems*, *13*(9).

Simmons, N., Myers, S., Morency, C., Chiang, A., & Knapp, D. (2021). Spiral: a multiresolution global tomography model of seismic wave speeds and radial anisotropy variations in the crust and mantle. *Geophysical Journal International*, *227*(2), 1366–1391.

Smith, M. L., & Dahlen, F. (1973). The azimuthal dependence of love and rayleigh wave propagation in a slightly anisotropic medium. *Journal of Geophysical Research*, *78*(17), 3321–3333.

Smyth, J. R., Miyajima, N., Huss, G. R., Hellebrand, E., Rubie, D. C., & Frost,

D. J. (2012). Olivine–wadsleyite–pyroxene topotaxy: Evidence for coherent nucleation and diffusion-controlled growth at the 410-km discontinuity. *Physics of the Earth and Planetary Interiors*, *200*, 85–91.

Stixrude, L., & Lithgow-Bertelloni, C. (2022). Thermal expansivity, heat capacity and bulk modulus of the mantle. *Geophysical Journal International*, *228*(2), 1119–1149.

Sturgeon, W., Ferreira, A. M., Faccenda, M., Chang, S.-J., & Schardong, L. (2019). On the origin of radial anisotropy near subducted slabs in the midmantle. *Geochemistry, Geophysics, Geosystems*, *20*(11), 5105–5125.

Wenk, H.-R., & Tomé, C. N. (1999). Modeling dynamic recrystallization of olivine aggregates deformed in simple shear. *Journal of Geophysical Research: Solid Earth*, *104*(B11), 25513–25527.

Yuan, K., & Beghein, C. (2013). Seismic anisotropy changes across upper mantle phase transitions. *Earth and Planetary Science Letters*, *374*, 132–144.

Zhou, W.-Y., Hao, M., Zhang, J. S., Chen, B., Wang, R., & Schmandt, B. (2022). Constraining composition and temperature variations in the mantle transition zone. *Nature communications*, *13*(1), 1–9.

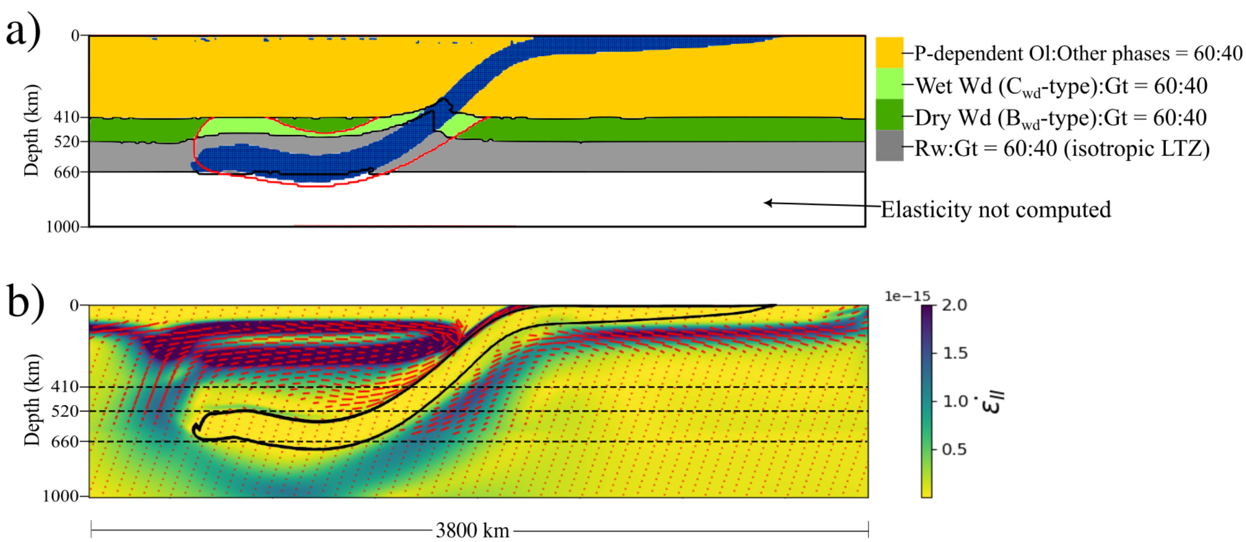

Figure 1. (a) Distribution of mineralogical fabrics across the subduction zone at the present day: Ol - olivine, Wd - wadsleyite, Gt - garnet, Rw - ringwoodite. In the upper transition zone, the distribution of hydrous and dry Wd is solely determined by the evolution of the 1750 K isotherm (solid red line) that encapsulates the slab (in blue). Solid black lines are the predicted topographies of the phase transition boundaries. For a fully dry UTZ, dark green shades associated with C_{wd}−type wadsleyite cover the entire UTZ. (b) Second invariant of the strain rate tensor $\dot{\varepsilon}_{II}$. Arrowless vectors correspond to the orientation of the finite strain ellipse.

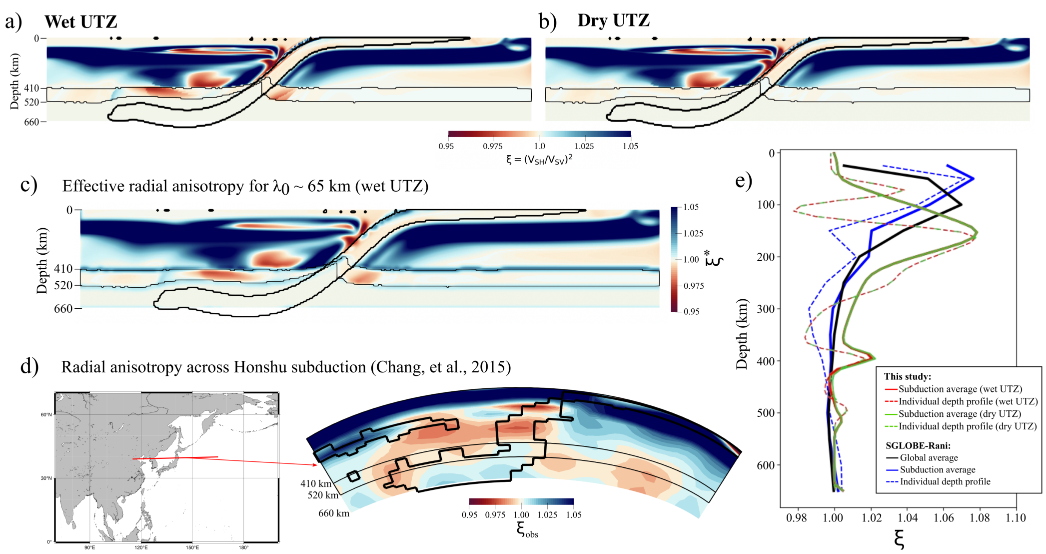

Figure 2. (a) Radial anisotropy $\xi = (V_{SH}/V_{SV})^2$ for a mantle model with a wet UTZ. (b) Same as (a) but for a dry UTZ. (c) Effective radial anisotropy ξ^* at $\lambda_0 = 65$ km for the wet UTZ model. The effective radial anisotropy in the case of a dry UTZ model is not shown since no significant anisotropy is produced. (d) Radial anisotropic tomography image across the Honshu arc retrieved from SGlobe-Rani Chang et al. (2015). (e) 1D radial anisotropy profiles from our model (in green and in red for dry and wet UTZ, respectively), across Honshu (in blue), and global average (in black). Individual depth profiles are taken at the back-arc basin. The choice of λ_0 is a conservative estimate for the wavelength of the SS phase sampling the upper mantle and the UTZ.

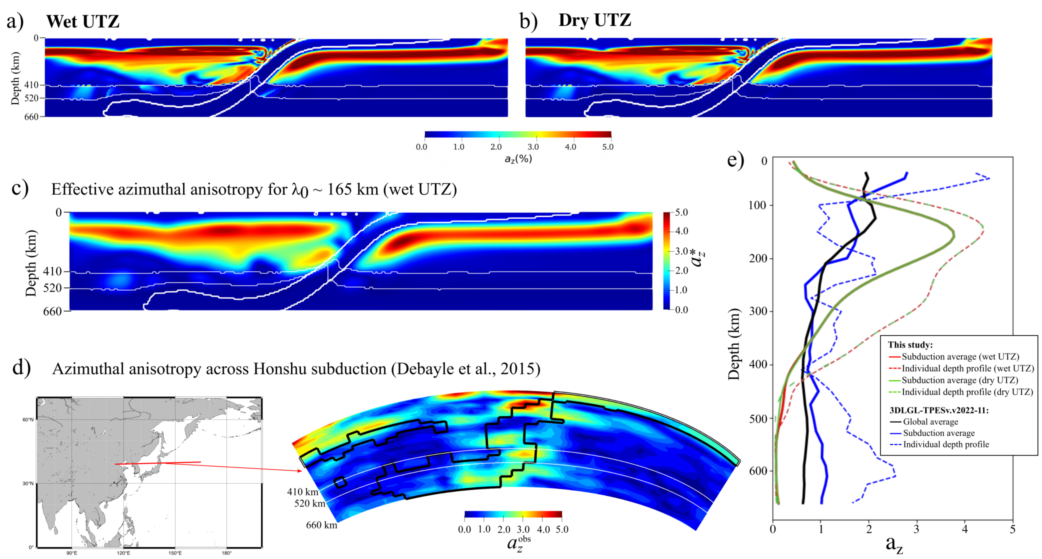

Figure 3. (a) Peak-to-peak azimuthal anisotropy a_z for a mantle model with a wet UTZ. (b) Same as (a) but for a dry UTZ. (c) Effective azimuthal anisotropy after homogenization a_z^* at λ_0 = 165 km for the wet UTZ model. Similarly, the effective azimuthal anisotropy in the case of a dry UTZ model is excluded as it produces near-zero amplitudes close to the slab. (d) Azimuthal anisotropic tomography image across the Honshu arc retrieved from 3DLGL-TPESv.v2022-11 Debayle et al. (2016). (e) 1D azimuthal anisotropy profiles from our model (in green and in red for dry and wet UTZ, respectively), across Honshu (in blue), and global average (in black). The chosen value of λ_0 roughly corresponds to the wavelength of first overtones with maximum sensitivity kernels at that same depth range.

Supplementary information for

On the influence of pressure, phase transitions, and water on large-scale seismic anisotropy underneath a subduction zone

John Keith Magali[1,2], Christine Thomas[1], Estelle Ledoux[3], Yann Capdeville[4], and Sébastien Merkel[2]

[1] *Institute of Geophysics, University of Müenster, Corrensstr. 24, 48149 Münster, Germany*

[2] *Univ. Lille, CNRS, INRAE, Centrale Lille, UMR 8207 - UMET - Unité Matériaux et Transformations, F-59000 Lille, France*

[3] *Department of Geology and Geophysics, University of Utah, Salt Lake City, UT, USA*

[4] *Laboratoire de Planétologie et Géodynamique, CNRS, UMR 6112, Université de Nantes, Nantes, France*

Contents of this file

Text S1 to S4

Figures S1 to S4

Text S1. Geodynamic modelling of intraoceanic subduction

To implement a 2-D geodynamic model of intra-oceanic subduction, we use the open software ASPECT (Kronbichler et al., 2012) that solves the conservation mass, momentum, and energy equations for an incompressible fluid and assume an infinite Prandtl number:

$$\nabla \cdot \mathbf{u} = 0, \tag{1}$$

$$-\nabla \cdot 2\eta_{\text{eff}}\dot{\varepsilon}(\mathbf{u}) + \nabla P = \rho \mathbf{g}, \tag{2}$$

$$\rho C_p \frac{DT}{Dt} - \nabla \cdot k \nabla T = H, \tag{3}$$

where $\frac{DT}{Dt}$ is the material derivative, and $\mathbf{u}$, η_{eff}, $\dot{\varepsilon}$, P, ρ, $\mathbf{g}$, C_p, T, and k are the velocity, effective viscosity, strain rate tensor, total pressure, density, gravitational acceleration, heat capacity, temperature, and thermal diffusivity, respectively. H refers to heat generation or consumption that takes into account adiabatic (through the extended Boussinesq approximation), latent, radiogenic, and shear heating effects.

We include four compositional fields reminiscent of Glerum et al. (2018): (a) overriding plate (OP), (b) subducting crust (SC), (c) subducting plate (SP), and (d) background mantle (M) whose time evolution follow an advection type equation. The computational domain is 6000 km $\times$ 1000 km and with adaptive mesh refinements incorporated, spatial resolutions vary from 5 km $\times$ 5 km across regions with sharp viscosity contrasts and across the slab up to 325 km $\times$ 325 km in regions of quiescence far from the slab.

The initial temperature field conforms to a half-space cooling model (Schubert et al., 2001) with a surface adiabatic temperature of 1573 K. The OP age evolves from 0 My at $x = 0$ km to 20 My at the trench ($x = 3000$ km). Meanwhile, the SP, initially dipping at 30°, age evolves from 0 My at $x = 6000$ km to 150 My at the trench. A linear mantle geotherm is then established from the lithosphere-asthenosphere boundary (LAB) to a depth of 1000 km. Fixed temperature boundary conditions are imposed at the top (293 K) and at the bottom (2100 K). Zero heat flux is imposed at the sidewalls. The initial compositional structure also follows an age-based plate model for OP and SP. A 7.5-km subducting crust is augmented to serve as a weak decoupling Newtonian layer. Free-slip boundary conditions are imposed across all boundaries. The initial setup is shown in Figure S1.

Text S1.1. Formulation of the viscoplastic rheology

We implement viscoplastic rheology where the viscoplastic effective viscosity η_{vp} is a harmonic average of viscous creeping and plastic yielding capped by a minimum and a maximum value, $\eta_{\mathrm{min}} = 1.0 \times 10^{20}$ Pa-s and $\eta_{\mathrm{max}} = 1.0 \times 10^{25}$ Pa-s, respectively:

$$\eta_{\mathrm{vp}} = \eta_{\mathrm{min}} + \left(\frac{1}{\eta_{\mathrm{max}}} + \frac{1}{\eta_{\mathrm{df/dl/pl}}} \right)^{-1}, \tag{4}$$

with:

$$\eta_{\mathrm{df/dl/pl}} = \left(\frac{1}{\eta_{\mathrm{df}}} + \frac{1}{\eta_{\mathrm{dl}}} + \frac{1}{\eta_{\mathrm{pl}}} \right)^{-1}. \tag{5}$$

The first two terms in Eq. (5) correspond to the effective viscosities due to diffusion and dislocation creeps (Karato and Wu, 1993):

$$\eta_{\mathrm{df/dl}} = \frac{1}{2} A^{-\frac{1}{n}} \dot{\varepsilon}_{II}^{\frac{1}{n}-1} \exp\left(\frac{E + PV}{nRT} \right), \tag{6}$$

where $\dot{\varepsilon}_{II}$ is the second invariant of the strain rate tensor, A is a prefactor, d is grain size, E and V are the activation energy and volume, P is hydrostatic pressure, R is gas constant, and T is temperature. The last term in Eq. (5) is the effective viscosity due to plastic yielding:

$$\eta_{\mathrm{pl}} = \frac{\sigma_y}{2\varepsilon_{II}}, \tag{7}$$

where the yield strength σ_y follows a Drucker Prager criterion (Davis and Selvadurai, 2005):

$$\sigma_y = C \cos\theta + P \sin\theta, \tag{8}$$

in which C is the cohesion, and θ is the internal friction angle. We set $\theta = 0$ for the weak decoupling layer which ensues a constant yield stress (von Mises criterion). Table 1 summarizes the viscoplastic rheology parameter values chosen in this study.

Text S1.2. Formulation of the effective mantle viscosity

To further promote slab stagnation, we implement a depth-dependent compositing model for the ambient mantle (Mitrovica and Forte, 1997) whose effective viscosity η_0 depends on depth z according to:

$$\eta_0(z) = \begin{cases} \eta_{\mathrm{min}} + (1.0 \times 10^{21}[\text{Pa-s}] - \eta_{\mathrm{min}}) \dfrac{z}{660[\text{km}]} & \text{if } z < 660 \text{ km} \\ 5.0 \times 10^{21}[\text{Pa-s}] & \text{if } x \geq 660 \text{ km} \end{cases}$$

Finally, the effective mantle viscosity η_{eff} is simply (Kronbichler et al., 2012):

$$\eta_{\text{eff}}(z, P, T, ..) = \eta_0(z)\frac{\eta_{\text{vp}}(P, T, ..)}{\eta_{\text{min}}} \tag{9}$$

Note that a viscosity jump by a factor of ~ 5 is implicitly defined at 660 km (Čížková et al., 2012; Agrusta et al., 2017). We do not consider the effect of crystallographic preferred orientation (CPO) strength on viscosity. Figure S1b illustrates the effective mantle viscosity at the final time step of the simulation.

Text S1.3. Modelling pressure-induced phase transformations

Following the method of Christensen and Yuen (1985), ASPECT employs an analytical phase function X to approximate the time evolution of a fraction of a material that underwent phase transformation and calculate the entropy change ΔS to calculate latent heat production. Both X and ΔS depend on the Clapeyron slope β_{410} (positive for an endothermic process and negative for an exothermic process), phase transition temperature T_{410}, phase transition width w, phase transition density contrasts $\Delta\rho_{410}$, and phase transition depths z_{410}. The aforementioned parameters are initialized in the material model plugin (see Table 2).

Text S2. Textures at selected locations across the subduction zone

We select several locations along independent pathlines to examine the orientations of the crystallographic axes in the evolved CPO of olivine (i.e. Figure S3a−g) and wadsleyite (Figure S3h−j) aggregates.

Text S3. Tomographic filtering through elastic homogenization

The foundation behind elastic homogenization can be found in the studies of Capdeville et al. (2010, 2015) and Capdeville and Métivier (2018), and its application to anisotropic media are detailed in Magali et al. (2021) and Magali et al. (2024) for $P-$independent and $P-$dependent fabrics, respectively. Elastic homogenization is based upon the minimum wavelength theory in seismology where small-scale heterogeneities in a 3-D medium with no scale separation such as

Table 1: Viscoplastic rheology parameters for each compositional field.

Parameter	Symbol	SC	SP	OP	M	Unit
Density	ρ	3150	3350	3350	3350	$\mathrm{kg \cdot m^{-3}}$
Thermal diffusivity	k	1.0×10^{-6}	1.0×10^{-6}	1.0×10^{-6}	1.0×10^{-6}	$\mathrm{m^2 \cdot s}$
Heat capacity	C_p	1250	1250	1250	1250	$\mathrm{J \cdot K^{-1} \cdot kg^{-1}}$
Dislocation creep						
Activation energy	E	0	5.4×10^5	4.3×10^5	4.3×10^5	$\mathrm{J \cdot mol^{-1}}$
Activation volume	V	0	2.0×10^{-5}	1.85×10^{-5}	1.5×10^{-5}	$\mathrm{mol^3 \cdot mol^{-1}}$
Prefactor	V	1.0×10^{-19}	2.4×10^{-16}	2.42×10^{-16}	3.91×10^{-15}	$\mathrm{Pa^{-n} \cdot s^{-1}}$
Stress exponent	n	1.0	3.5	3.0	3.0	–
Diffusion creep						
Activation energy	E	0	3.0×10^5	2.4×10^5	2.4×10^5	$\mathrm{J \cdot mol^{-1}}$
Activation volume	V	0	5.0×10^{-6}	5.0×10^{-6}	2.5×10^{-6}	$\mathrm{mol^3 \cdot mol^{-1}}$
Prefactor	V	1.0×10^{-19}	6.08×10^{-14}	6.08×10^{-14}	3.74×10^{-14}	$\mathrm{Pa^{-n} \cdot s^{-1}}$
Plastic yielding						
Cohesion	C	1.0×10^{15}	1.0×10^6	1.0×10^{15}	1.0×10^6	MPa
Internal friction angle	θ	0	20	0	20	$^\circ$

"SC" stands for the subducting crust, "SP" for the mantle part of the subducting plate, "OP" for the overriding plate, and "M" the background mantle.
Values are loosely based on Hirth and Kohlstedf (2003).
Other input parameters in the viscoplastic material model of ASPECT are set to their default values unless otherwise specified.

Table 2: Phase transition parameters at the 410 km seismic discontinuity.

Parameter	410 km	520 km	660 km	Unit
Clapeyron slope	2.55×10^6	5.05×10^6	-2.07×10^6	$\mathrm{Pa \cdot K^{-1}}$
Density contrast	370	130	320	$\mathrm{kg \cdot m^{-3}}$
Phase transition width	10	10	10	km
Phase transition temperature	1750	1850	1900	K

Density contrast corresponds to the expected density of a pyrolitic composition.

the true Earth are replaced with effective properties when:

$$k_{\max} = \frac{1}{\epsilon_0 \lambda_0}, \tag{10}$$

where $k_{\max}$ is the maximum wavenumber of the heterogeneities, λ_0 is the minimum wavelength of the observed wavefield, and ϵ_0 is the scale separation constant which we set to $\epsilon_0 = 0.5$. Capdeville and Métivier (2018) numerically verified that seismic tomography can be represented by an operator $\mathcal{H}$ that when applied to an elastic medium $\mathbf{S}$, the resulting effective medium $\mathbf{S}^*$ is the best possible model one could obtain from seismic tomography assuming perfect data coverage:

$$\mathbf{S}^* = \mathcal{H}^{\lambda_0}(\mathbf{S}). \tag{11}$$

Of course in the limit $\lambda_0 \to 0$, that is a wavefield with an infinite frequency band, one obtains the true structure $\mathbf{S}$ assuming a homogeneous distribution of source-receiver pairs.

One method to test the reliability of our anisotropy model is by comparing it with anisotropic tomography images of a subduction zone. To date, SGlobe-Rani Chang et al. (2015) and 3DLGL-TPESv.v2022-11 Debayle et al. (2016) are two of the most comprehensive global anisotropy models with the former having over 100,000 free-surface reflected S waves as data that help to constrain transition zone structures, and the latter having over 2,000,000 Rayleigh wave observations up to the fifth overtone to constrain azimuthal anisotropy at upper and mid-mantle depths. In our work, we compare our results with tomographic images of the Honshu subduction zone whose subduction style and implied geometry resemble our geodynamic model of intraoceanic subduction.

Text S4. Expressions for large-scale seismic anisotropy

Once the effective medium is obtained, we use two parameters that are often recovered from anisotropic tomography as means to describe our anisotropy models namely, $S-$wave radial anisotropy ξ, and peak-to-peak azimuthal anisotropy a_z.

In a weakly anisotropic medium, Montagner and Nataf (1986) showed that ξ is simply the radial anisotropy associated with an azimuthally-average vertically transverse isotropic (VTI) medium whose elastic constants N and L relate to ξ through:

$$\xi = \frac{N}{L}, \tag{12}$$

where:

$$N = \frac{1}{8}(S_{11} + S_{22}) - \frac{1}{4}S_{12} + \frac{1}{2}S_{66}) \tag{13}$$

$$L = \frac{1}{2}(S_{55} + S_{66}). \tag{14}$$

Likewise, a_z describes horizontally-propagating SV waves in a horizontally-transverse isotropic (HTI) medium. It depends on elastic constants G_c and G_s through:

$$a_z = 2\frac{G_c^2 + G_s^2}{L}, \tag{15}$$

where:

$$G_c = \frac{1}{2}(S_{55} - S_{44}) \tag{16}$$

$$G_s = S_{54}. \tag{17}$$

Effective radial and azimuthal anisotropies across the subduction zone are shown in Figures S4 and S5, respectively, at several homogenization wavelengths: $\lambda_0 = [10\text{ km}, 50\text{ km}, 100\text{ km}, 200\text{ km}]$.

References

Agrusta, R., Goes, S., and Van Hunen, J. (2017). Subducting-slab transition-zone interaction: Stagnation, penetration and mode switches. *Earth and Planetary Science Letters*, 464:10–23.

Capdeville, Y., Guillot, L., and Marigo, J.-J. (2010). 2-d non-periodic homogenization to upscale elastic media for p–sv waves. *Geophysical Journal International*, 182(2):903–922.

Capdeville, Y. and Métivier, L. (2018). Elastic full waveform inversion based on the homogenization method: theoretical framework and 2-d numerical illustrations. *Geophysical Journal International*, 213:1093–1112.

Capdeville, Y., Zhao, M., and Cupillard, P. (2015). Fast fourier homogenization for elastic wave propagation in complex media. *Wave Motion*, 54:170–186.

Chang, S.-J., Ferreira, A. M., Ritsema, J., van Heijst, H. J., and Woodhouse, J. H. (2015). Joint inversion for global isotropic and radially anisotropic mantle structure including crustal thickness perturbations. *Journal of Geophysical Research: Solid Earth*, 120(6):4278–4300.

Christensen, U. R. and Yuen, D. A. (1985). Layered convection induced by phase transitions. *Journal of Geophysical Research: Solid Earth*, 90(B12):10291–10300.

Čížková, H., van den Berg, A. P., Spakman, W., and Matyska, C. (2012). The viscosity of earth's lower mantle inferred from sinking speed of subducted lithosphere. *Physics of the earth and Planetary Interiors*, 200:56–62.

Davis, R. O. and Selvadurai, A. P. (2005). *Plasticity and geomechanics*. Cambridge university press.

Debayle, E., Dubuffet, F., and Durand, S. (2016). An automatically updated s-wave model of the upper mantle and the depth extent of azimuthal anisotropy. *Geophysical Research Letters*, 43(2):674–682.

Dziewonski, A. M. and Anderson, D. L. (1981). Preliminary reference earth model. *Physics of the earth and planetary interiors*, 25(4):297–356.

Glerum, A., Thieulot, C., Fraters, M., Blom, C., and Spakman, W. (2018). Nonlinear viscoplasticity in aspect: benchmarking and applications to subduction. *Solid Earth*, 9(2):267–294.

Hirth, G. and Kohlstedf, D. (2003). Rheology of the upper mantle and the mantle wedge: A view from the experimentalists. *Geophysical monograph-american geophysical union*, 138:83–106.

Karato, S.-i. and Wu, P. (1993). Rheology of the upper mantle: A synthesis. *Science*, 260(5109):771–778.

Kronbichler, M., Heister, T., and Bangerth, W. (2012). High accuracy mantle convection simulation through modern numerical methods. *Geophysical Journal International*, 191(1):12–29.

Magali, J. K., Bodin, T., Hedjazian, N., Ricard, Y., Capdeville, Y., and Debayle, E. (2021). Quantifying intrinsic and extrinsic contributions to radial anisotropy in tomographic models. *Journal of Geophysical Research: Solid Earth*, 126(10):e2021JB022322.

Magali, J. K., Ledoux, E. E., Thomas, C., Capdeville, Y., and Merkel, S. (2024). Pressure-dependent large-scale seismic anisotropy induced by non-Newtonian mantle flow. *Geophysical Journal International*, page ggae165.

Mitrovica, J. X. and Forte, A. M. (1997). Radial profile of mantle viscosity: Results from the joint inversion of convection and postglacial rebound observables. *Journal of Geophysical Research: Solid Earth*, 102(B2):2751–2769.

Montagner, J.-P. and Nataf, H.-C. (1986). A simple method for inverting the azimuthal anisotropy of surface waves. *Journal of Geophysical Research: Solid Earth*, 91(B1):511–520.

Schubert, G., Turcotte, D. L., and Olson, P. (2001). *Mantle convection in the Earth and planets*. Cambridge University Press.

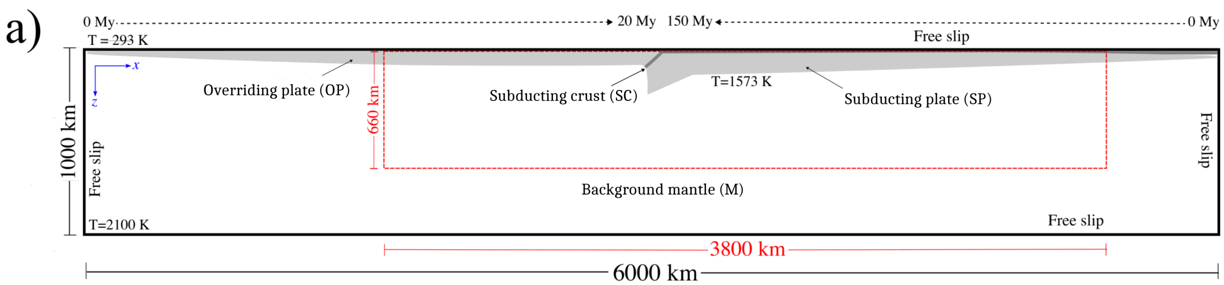

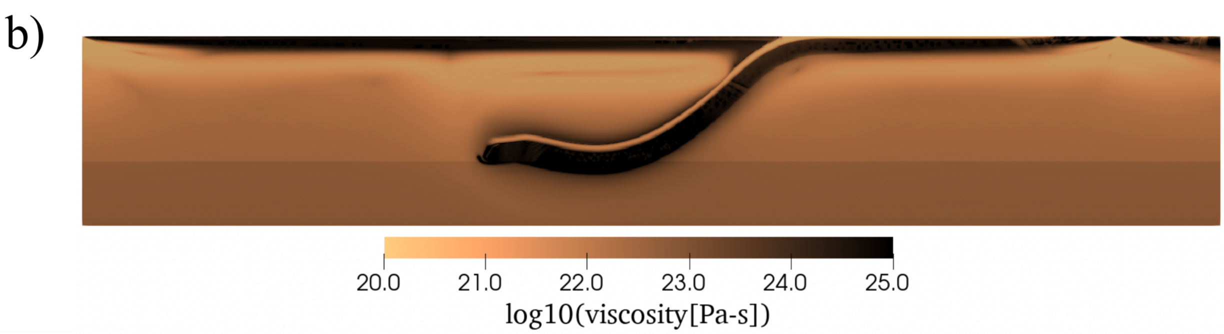

Figure S1: a.) Initial and boundary conditions, and simulation domain of our 2-D geodynamic model. Four compositional fields with distinct rheological properties are included namely, subducting plate (SP), subducting crust (SC), overriding plate (OP), and the background mantle (M) whose evolution follow an advection equation. The initial temperature field follows an age-based plate cooling model that increases from the leftmost part of the modelling domain to 20 My for the OP, and from the rightmost part to 150 My for the SP. Fixed temperature boundary conditions are imposed at the top (293 K) and at the bottom (2100 K). Free slip is imposed on all sides. Red box corresponds to the domain at which we calculate seismic anisotropy. b.) Effective mantle viscosity at the present day in log[Pa-s] units.

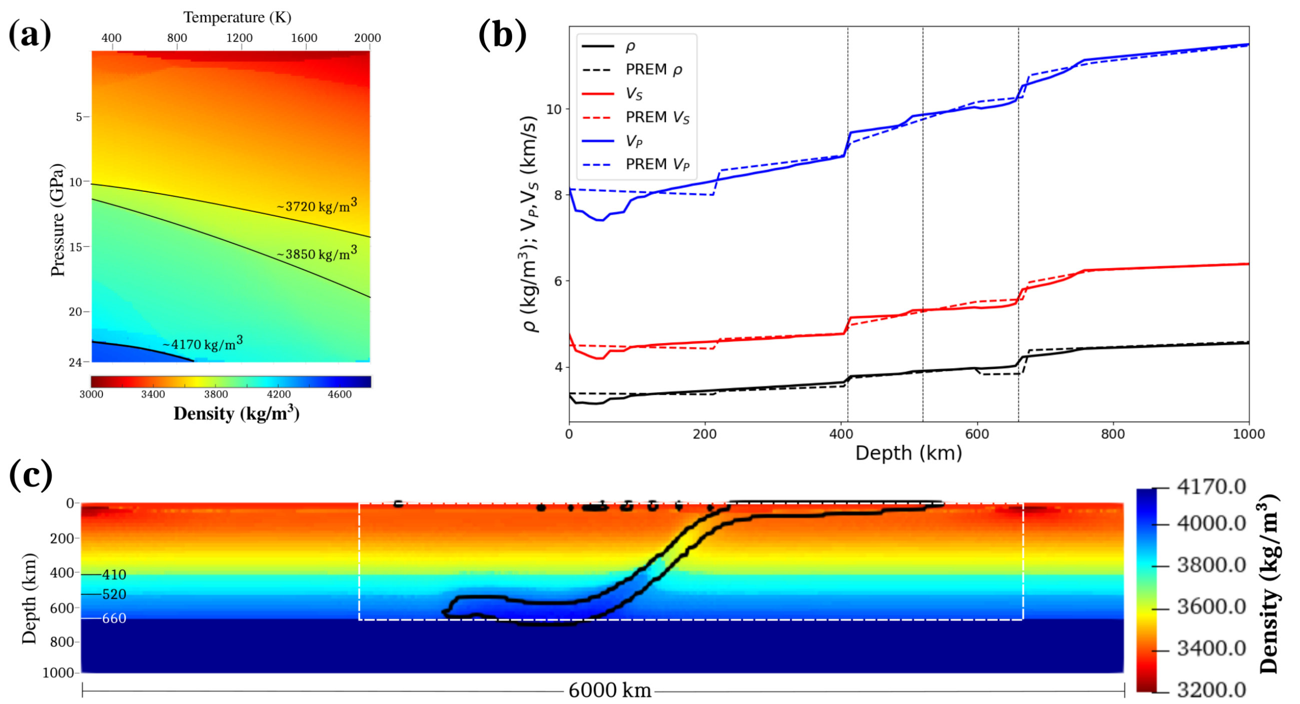

Figure S2: (a) Density map predicted from Perple_X for a pyrolitic mantle composition. Black contour lines correspond to arbitrary density crossovers associated with the following phase transitions: Olivine → wadsleyite (∼3720 $\mathrm{kg \cdot m^3}$), wadsleyite → ringwoodite (∼3850 $\mathrm{kg \cdot m^3}$), and ringwoodite → bridgmanite (∼4170 $\mathrm{kg \cdot m^3}$). (b) Predicted 1D density, V_P and V_S structure of pyrolite (solid lines) versus the preliminary reference Earth model, PREM (Dziewonski and Anderson, 1981) (dashed lines). (c) Density structure of our subduction model at the present time using (a). White dashed rectangle corresponds to the region at which seismic anisotropy is calculated. Solid black lines delineate the subducting slab.

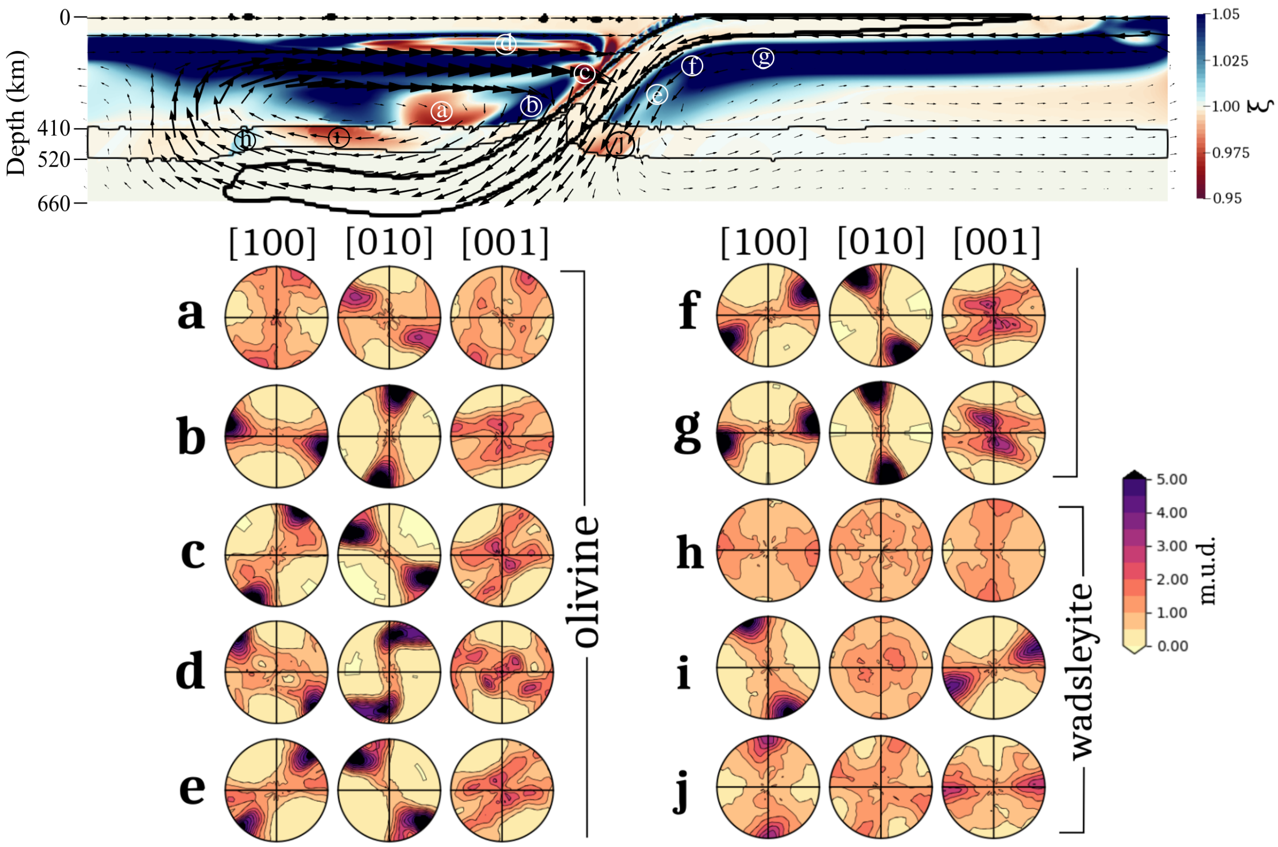

Figure S3: Top panel: Predicted large-scale radial anisotropy ($\xi = V_{SH}^2/V_{SV}^2$) across a stagnating oceanic lithospheric slab (solid black line). Solid gray lines delineate the presumed topography of the 410 and 520-km seismic discontinuities assuming a pyrolitic mantle. Arrows represent mantle flow velocity at the final time step. Bottom panel: Computed $P-$dependent olivine and hydrous wadsleyite aggregate textures at selected locations along the model, *a-g* for olivine and *h-j* for wadsleyite, respectively. M.u.d. refers to the multiples of uniform distribution which measures texture strength.

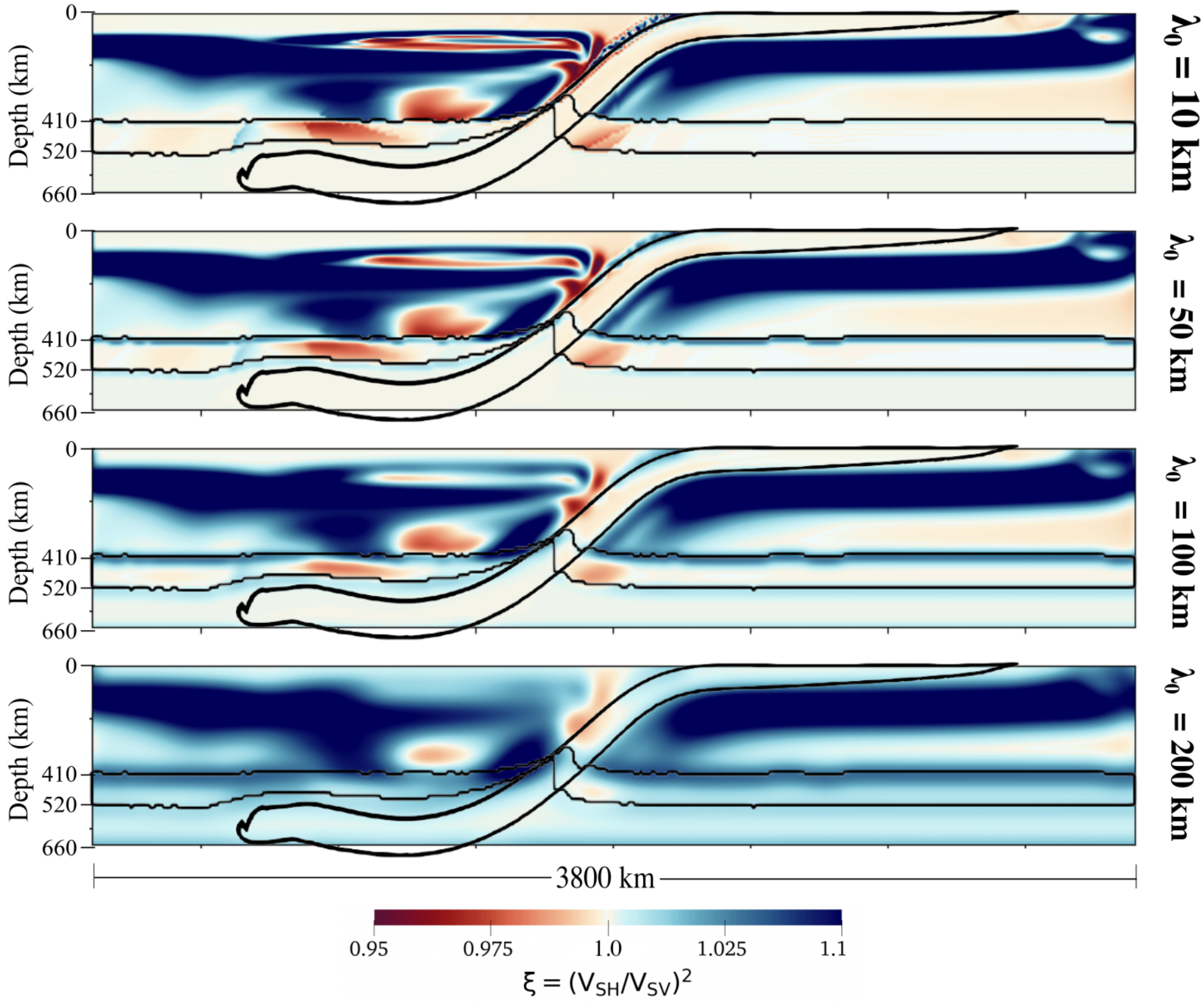

Figure S4: Effective radial anisotropy at varying homogenization wavelengths.

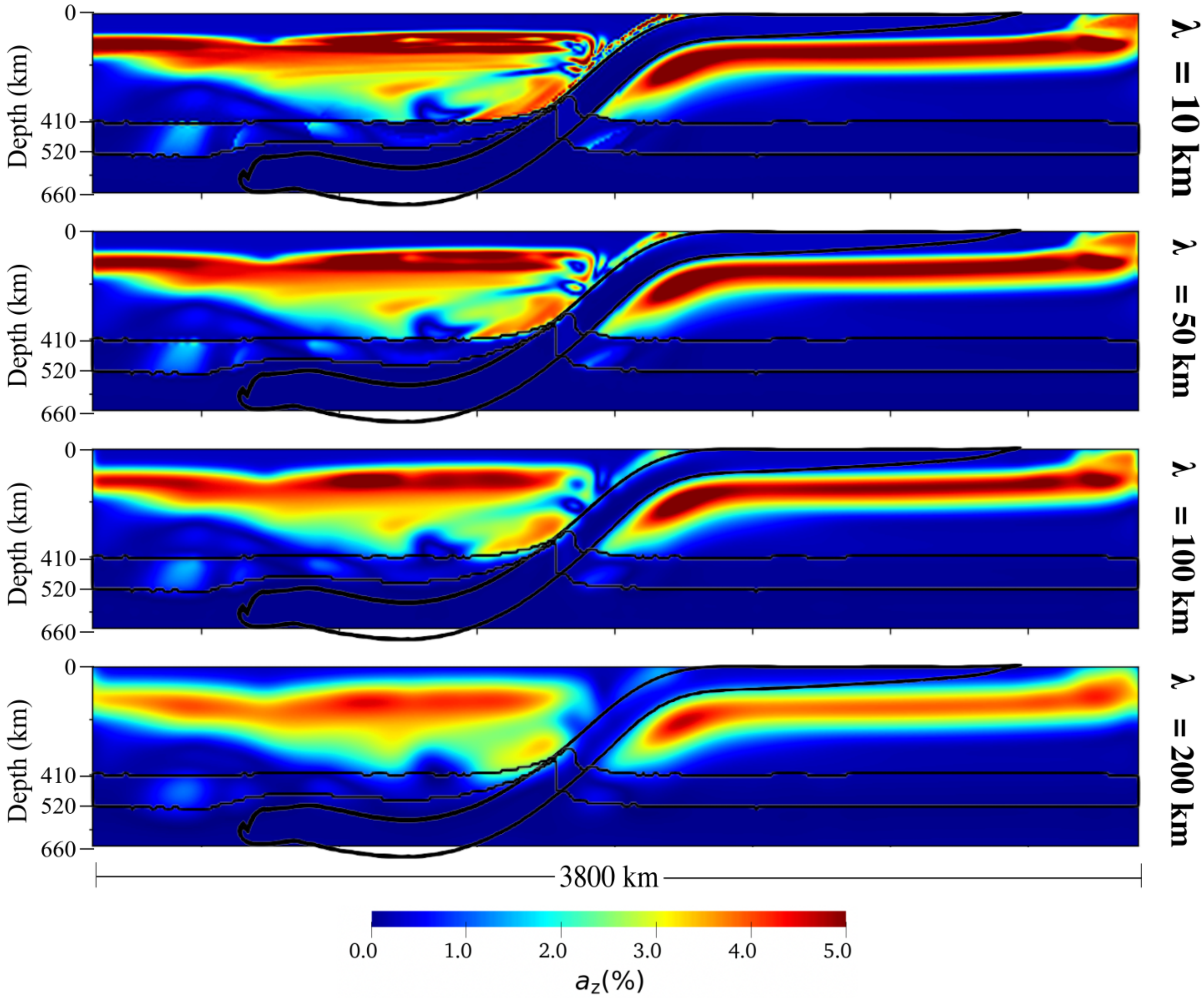

Figure S5: Effective azimuthal anisotropy at varying homogenization wavelengths.